Diagnostic-based modeling on a micro-scale atmospheric-pressure plasma jet*

Jochen Waskoenig[1], Kari Niemi[1], Nikolas Knake[2],
Lucy Marie Graham[1], Stephan Reuter[1],
Volker Schulz-von der Gathen[2], and Timo Gans[1,‡]

[1]*Centre for Plasma Physics, Queen's University Belfast, Belfast BT7 1NN,
Northern Ireland, UK;* [2]*Institute for Experimental Physics II: Applied Plasma
Physics, Ruhr-Universität Bochum, 44801 Bochum, Germany*

Abstract: Diagnostic-based modeling (DBM) actively combines complementary advantages of numerical plasma simulations and relatively simple optical emission spectroscopy (OES). DBM is applied to determine spatial absolute atomic oxygen ground-state density profiles in a micro atmospheric-pressure plasma jet operated in He–O_2. A 1D fluid model with semi-kinetic treatment of the electrons yields detailed information on the electron dynamics and the corresponding spatio-temporal electron energy distribution function. Benchmarking this time- and space-resolved simulation with phase-resolved OES (PROES) allows subsequent derivation of effective excitation rates as the basis for DBM. The population dynamics of the upper $O(3p^3P)$ oxygen state ($\lambda = 844$ nm) is governed by direct electron impact excitation, dissociative excitation, radiation losses, and collisional induced quenching. Absolute values for atomic oxygen densities are obtained through tracer comparison with the upper $Ar(2p_1)$ state ($\lambda = 750.4$ nm). The resulting spatial profile for the absolute atomic oxygen density shows an excellent quantitative agreement to a density profile obtained by two-photon absorption laser-induced fluorescence spectroscopy.

Keywords: atomic oxygen; atmospheric pressure; laser spectroscopy; numerical simulation; optical emission spectroscopy.

INTRODUCTION

Radio-frequency (RF)-driven micro-scale atmospheric-pressure plasma jets (µAPPJs) operated with He–O_2 feed gas provide high densities of reactive oxygen species and radicals at low gas temperatures. These discharges promise high potential for technological exploitation. Of particular interest is the treatment of sensitive surfaces in biomedicine [1–4].

Vital for the development and optimization of such plasma sources is the understanding of the fundamental mechanisms. Key aspects are the energy dissipation and transport processes particularly in the interface region between the core plasma and the post discharge effluent, as illustrated in Fig. 1. In general, the plasma chemistry inside the discharge volume is strongly influenced by the dynamics of the plasma boundary sheaths as well as by the processes at the electrode surfaces. Electrons energized in the sheath regions dominate the electron-impact excitation and ionization in the core plasma.
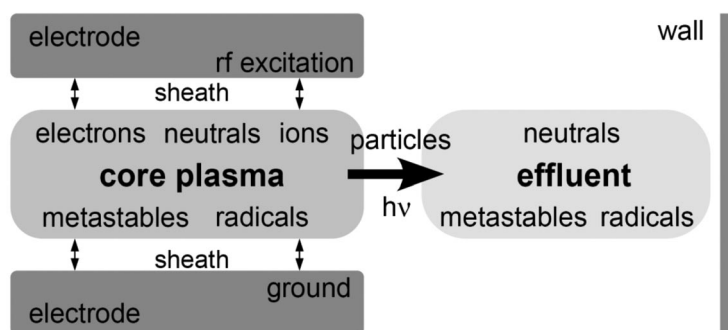
Fig. 1 Sketch of the dynamics in the core plasma and energy transport mechanisms from the core to the effluent region. The wall represents a surface to be treated in technological applications.

Subsequent Penning ionization and three-body collisions also play important roles in the particle and power balance, since the environment is highly collisional. The effluent region, in contrast, is practically free of charged particles [5]. Nevertheless, a significant amount of energy is transported in this region by reactive atoms, radicals, excited particles, as well as by radiation [6–9].

Quantitative determination of individual particle densities and fluxes provides important net information. For atomic oxygen—a key-role species in most applications—there are three methods predominantly used: two-photon absorption laser-induced fluorescence spectroscopy (TALIF) [10,11], actinometry [12–14], and numerical simulation [8,15]. Quantitative TALIF measurements of atomic oxygen densities in the regions of the post-discharge effluent [11,16,17] and the core-plasma [18] have been reported. Although providing direct access to the atomic ground state, it is an experimentally intricate technique that, furthermore, is limited to discharge designs providing extensive optical access. Actinometry represents a much less demanding method [12] that is commonly applied in the low-pressure regime [13,14]. However, the conceptual conditions for this optical emission-based technique are not given in the case of the non-thermal atmospheric-pressure plasmas considered here. Pure modeling of the plasma chemistry at atmospheric pressure is challenging due to the multitude of reaction paths with partly vague known or even ill-defined reaction rates, in particular for three-body collisions and surface interactions. The validity of global models [15] is questionable, since the pronounced electron dynamics [7,19,20] in such RF-driven micro discharges is not explicitly taken into account.

In this article, the recently introduced method of diagnostic-based modeling (DBM) [21,22] for the determination of absolute atomic oxygen densities in the core of a µAPPJ is described in more detail. DBM combines easy-to-apply optical emission spectroscopy (OES) with a relatively simple 1D numerical simulation that only comprises a basic set of plasma reactions (17 in total), while the numerous chemical reactions running on a longer time scale are not taken into account. The optical emission signal intrinsically contains information about all chemical reactions in the discharge. The simulation only needs to account for electron processes affecting the electron energy distribution function (EEDF) in the threshold range of the observed excited states. As a consequence, DBM exploits the complementary strengths of both techniques.

The model is based on iteratively solving the fluid equations for the different species, where the electrons are treated semi-kinetically, and Poisson's equation, respectively, until consistency is reached. The kinetic reaction rates and electron transport coefficients are calculated by means of a two-term approximation Boltzmann solver [23]. In the following, several aspects are discussed: the ion drift diffusion approximation, the boundary conditions, the particle fluxes toward the electrodes, and the resulting secondary electron emission. The method used for assigning the external electrical power input instead of the voltage or current input is explained. Its capability of covering the α- to γ-mode transition and its implementation into the self-consistent model is described.

The model predictions for the properties of energetic electrons are benchmarked by comparing the simulated spatio-temporal characteristics of the argon optical emission line $\lambda = 750.4$ nm ($2p_1 \rightarrow 1s_2$) with corresponding results of phase-resolved OES (PROES) measurements. The agreement is very good, and the resulting three structures can be designated to sheath expansion, sheath collapse, and secondary electron multiplication in the plasma boundary sheath initiated by heavy particle impact onto the electrodes as well as Penning ionization in the volume. A possible explanation for the remaining discrepancy in the plasma bulk region is given.

The DBM results for the O-atom density along the discharge channel, obtained as an average over time and over the space across the 1-mm electrode gap, are compared to on-axis TALIF findings obtained in a similar μAPPJ set-up with a 2-mm gap [18]. The results of the completely independent methods agree remarkably well.

TALIF MEASUREMENTS IN THE EFFLUENT

The μAPPJ consists of two planar stainless steel electrodes of 30 mm length, 1 mm thickness, and 1 mm distance inside a quartz glass cuvette. One electrode is grounded, the other one is driven at 13.56 MHz. Between the electrodes, a helium gas flow with an admixture of 1 % oxygen is applied, resulting in a cold jet-like glow-mode plasma. The discharge is based on the concept of the APPJ introduced by Selwyn, Hicks, and co-workers [5,24]. Here, it is scaled down and optimized for ideal optical access due to the large optical solid angle provided by the quartz cuvette design. The downscaled discharge dimensions ($1 \times 1 \times 30$ mm^3) significantly reduce the gas flow (1 slm), keeping the gas velocity in the same range of some 10 ms^{-1}. Details of the design can be found in refs. [7,17]. This simple co-planar geometry is also ideally suited for computational simulation.

The atomic oxygen density in the effluent has been measured by TALIF spectroscopy. Tunable UV laser radiation is used to excite oxygen ground-state atoms by simultaneous absorption of two UV photons ($\lambda = 225$ nm). The fluorescence radiation emitted when the atoms revert to an energetically lower state is measured in order to gain information about the atomic oxygen density. The measurements are calibrated with TALIF measurements on xenon, according to earlier investigations on the concentric APPJ [11]. Collisional quenching, temperature effects, and vignetting of the signal are essential aspects to be considered in the analysis of the measurements [11,16]. Figure 2 shows the spatial ground-state atomic oxygen density distribution in the effluent of such a μAPPJ [17]. Here, z denotes the distance from the nozzle in direction of the gas flow, and y the distance from the jet's axis normal to the electrode surfaces. The highest atomic oxygen density of 2×10^{14} cm^{-3} is measured on-axis directly at the nozzle. A confined stream reaches out several centimeters where atomic oxygen densities of some 10^{13} cm^{-3} can be found. The lowest densities are detected directly in front of the jet's elec-
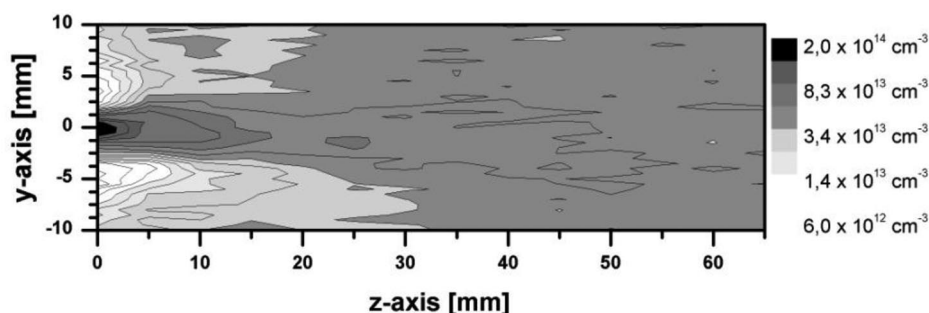

Fig. 2 2D spatial distribution of absolute densities of ground-state atomic oxygen in the effluent of the μAPPJ obtained by TALIF in He with 1 % O admixture.

trodes, where vortices of the gas flow are present. These vortices, the widening of the gas stream and mixing with outer atmosphere, impede further understanding of the underlying processes.

Thus, to understand the oxygen chemistry of the µAPPJ, it is mandatory to investigate and observe the creation and destruction processes for the reactive oxygen species also inside the discharge core itself [18].

OES MEASUREMENTS IN THE DISCHARGE REGION

For the determination of the atomic oxygen density within the discharge region by DBM, optical emission spectra of the core plasma are recorded using a sensitivity calibrated spectrograph covering a wavelength range from 430 to 950 nm with a full width at half maximum (FWHM) resolution of 0.5 nm. The light emission is collected through the quartz windows of the jet via an optical fiber positioned perpendicular to the plasma channel. The effective spatial resolution of the system was measured to be about 1.4 mm. The integration time is in the order of several hundred milliseconds to seconds. The recorded spectra are, therefore, time- and space-averaged across the discharge gap.

Optical parameters influencing the signal such as observation volume and solid angle can be taken into account by normalizing the measured optical emission from atomic oxygen to the emission signal from an inert gas. This tracer gas is admixed in a defined quantity, small enough ($\leq$0.1 %) to exclude a disturbance of the plasma. In this study, the argon optical emission line from the $Ar(2p_1)$ state at $\lambda =$ 750.4 nm is chosen.

This concept is analogous to the classical actinometry approach, where optical transitions from excited states only populated by electron-impact excitation from the ground state are used. These states are assumed to be only depopulated by radiation and not by collisional quenching [12]. Actinometry is furthermore based on the assumption that the electron-impact excitation cross-sections of the two compared species have the same shape and threshold. When these conditions are met, the ratio of the excitation rates is independent of the plasma conditions. Classical actinometry can provide a qualitative measurement of the atomic oxygen ground-state density in low-pressure plasmas with not too low degree of dissociation [13]. However, the determination of absolute atomic oxygen densities in cold atmospheric-pressure plasmas is significantly more complex. Collisional-induced quenching of the upper $O(3p^3P)$ and $Ar(2p_1)$ states outbalances the optical transition rates and thus needs to be taken into account: The effective optical branching ratios of the corresponding transitions are calculated using the natural lifetime of the excited state and the quenching coefficients for the feed gas composition according to $a_{ik} = A_{ik}/(A_i + \Sigma_q k_{iq}n_q)$. A_i is the sum of all optical transition probabilities A_{ik} for the excited state k, and is equal to the reciprocal of the natural lifetime τ_0. k_{iq} denotes the quenching rate coefficient for a partial density n_q of a specific collider species q [11,25]. The excited states chosen for this study have one dominant optical transition. For the present case, therefore, A_i is equal to A_{ik}. The quenching coefficients and the collider densities are temperature-dependent. The gas temperature (330 ± 15 K) is determined spectroscopically from rotational band emission spectra of residual molecular nitrogen impurities.

The thresholds for direct electron-impact excitation of $O(3p^3P)$ at 10.98 eV and of $Ar(2p_1)$ at 13.48 eV differ by 2.5 eV according to the cross-section data [26–28]. At atmospheric pressure, however, this small threshold difference has a significant influence on the excitation rate ratio due to considerable variations of the electron energy distribution in this energy range.

Figure 3 shows the ratio of the excitation rates $k_{Ar,e}/k_{O,e}$ as a function of mean electron energy calculated with different EEDFs: The upper curve shows the excitation rate ratio using a simple Maxwellian EEDF, the lower curve is based on solving the Boltzmann equation using the two-term approximation. The dashed lines indicate the effective ratio of 0.32 and the mean electron energy of 1.4 eV derived from the time- and space-dependent numerical simulation discussed below. The ratio of the excitation rates for both the Maxwellian and the two-term EEDF is strongly dependent on the energy. Unlike in actinometry, a constant ratio of the direct excitation rates, i.e., a ratio independent of the
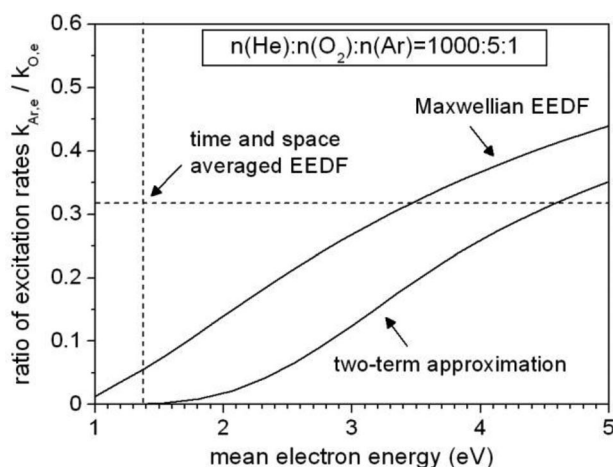
Fig. 3 Calculated ratio of direct excitation rates of $Ar(2p_1)$ and $O(3p^3P)$ assuming a Maxwellian EEDF, an EEDF calculated using a two-term approximation Boltzmann solver, and the effective ratio of the direct excitation rates (dashed lines) derived from time- and space-averaged EEDF for DBM.

plasma conditions, cannot be assumed. The ratio of the rate coefficients depends on the slope of the EEDF in the thresholds regime. Therefore, the Maxwellian EEDF always yields a larger value for the ratio than the more Druyvesteyn-like convex-shaped two-term approximation EEDF. For the evaluation of time- and space-integrated measurements, the pronounced temporal and spatial electron dynamics need to be considered. Therefore, detailed information on the EEDF in the relevant energy range is required for quantitative density determination. Here, this is obtained by a 1D numerical simulation across the discharge gap of the μAPPJ.

Numerical simulation

Since both electrodes of the μAPPJ have an identical surface area, and are capped with dielectric windows along the sides, the discharge produces a symmetric capacitively coupled RF plasma without dc-selfbias: the electron processes occur symmetrically with respect to the center of the electrode gap, but they are shifted in time by half of the RF period. In addition, the length of the jet is large compared to the electrode gap. This offers a model approach that considers only the spatial dimension across the discharge gap.

   This relatively simple 1D numerical simulation yields the electron dynamics within the discharge core of the μAPPJ. The atmospheric-pressure plasma is simulated in a He–O_2 (1000:5) gas mixture at a gas temperature of 345 K. The number of considered species (He, He^*, He^+, He_2^*, He_2^+, O_2, O_2^+) and reactions (17 in total) are purposely kept minimum. The measured optical emission signal implicitly yields information on the plasma chemistry and resulting atomic oxygen densities. Since only the slope in the relevant energy range of the excitation thresholds is required, a rather simple numerical simulation of the electron properties without inclusion of a large number of chemical reactions is sufficient. Table 1 shows the elementary reactions accounted for in the simulation. A significantly extended model including additional species (O, O^+, O^-, O_3) and corresponding reactions (overall, 57 reactions) was used to verify the simple model: The differences regarding the simulated electron dynamics turn out to be negligible.

Table 1 Elementary reactions and corresponding rate constants.

No.	Reaction[a]	Rate constant[b]	Ref.
R1	$e + He \rightarrow He + e$	$f(\varepsilon)$	[23]
R2	$e + He \rightarrow He^* + e$	$f(\varepsilon)$	[23]
R3	$e + He \rightarrow He^+ + 2e$	$f(\varepsilon)$	[23]
R4	$e + He^* \rightarrow He^+ + 2e$	$f(\varepsilon)$	[23]
R5	$e + He^* \rightarrow He + e$	$1.099 \times 10^{-17} T_\varepsilon^{0.31}$	[29]
R6	$e + He_2^* \rightarrow He_2^+ + e$	$1.268 \times 10^{-18} T_\varepsilon^{0.71} \exp(-39\,450/T_\varepsilon)$	[29]
R7	$e + He_2^+ \rightarrow He^* + e$	$4.624 \times 10^{-11} T_\varepsilon^{-1.5}$	[30]
R8	$He^* + He^* \rightarrow He + He^+ + e$	2.7×10^{-16}	[29]
R9	$He^* + He^* \rightarrow He_2^+ + e$	1.5×10^{-15}	[30]
R10	$He^* + 2He \rightarrow He_2^* + He$	2.0×10^{-46} m^6/s	[30]
R11	$He_2^* + M \rightarrow 2He + M$	1.0×10^4/s	[30]
R12	$He_2^* + He_2^* \rightarrow 2He + He_2^+ + e$	1.5×10^{-15}	[30]
R13	$He_2^* + 2He \rightarrow He_2^+ + He$	1.1×10^{-43} m^6/s	[30]
R14	$e + O_2 \rightarrow O_2 + e$	$f(\varepsilon)$	[23]
R15	$e + O_2 \rightarrow O_2^+ + 2e$	$f(\varepsilon)$	[23]
R16	$He^* + O_2 \rightarrow He + O_2^+ + e$	2.54×10^{-16}	[31]
R17	$He^+ + O_2 \rightarrow O_2^+ + He$	3.3×10^{-17}	[31]

[a]M in reaction R11 denotes an arbitrary collision partner.
[b]Units: Rate constants in m^3/s unless otherwise noted. T_ε in K. $f(\varepsilon)$ indicates that the rate constant is calculated on the basis of the two-term approximation EEDF as a function of the mean electron energy.

The model is based on fluid equations with a semi-kinetic treatment of the electrons. This means that the transport coefficients and reaction rates for electron impact collisions are obtained using a 0D Boltzmann solver in the two-term approximation [23]. These rates and transport coefficients are fitted to analytical functions dependent on the mean electron energy. The latter one is solved in the 1D model. The governing equations are mass conservation (eq. 1) and momentum conservation (eq. 2) for all species as well as the electron energy conservation (eq. 3). The set of coupled differential equations is closed by Poisson's equation (eq. 4):

$$\frac{\partial n_i}{\partial t} = -\vec{\nabla}\vec{\Gamma}_i + \sum_j n_i n_j k_{ji} \tag{1}$$

$$\vec{\Gamma}_{ch} = \mp n_{ch}\, \mu_{ch}\vec{E} - D_{ch}\vec{\nabla}n_{ch} \quad ; \quad \vec{\Gamma}_n = -D_n\vec{\nabla}n_n \tag{2}$$

$$\frac{\partial}{\partial t}(n_e\varepsilon) = -\vec{\nabla}\vec{\Gamma}_\varepsilon - e\vec{\Gamma}_e\vec{E} - \sum_j n_e n_j k_{L,je} - 3\frac{m_e}{m_{He}}k_b v_m n_e\left(T_e - T_g\right) \tag{3}$$

where $\quad \vec{\Gamma}_\varepsilon = \dfrac{5}{3}\vec{\Gamma}_e - \dfrac{5}{3}n_e D_e\vec{\nabla}\varepsilon$

$$\Delta\varphi = -\frac{1}{\varepsilon_0}\sum_{ch} q_{ch} n_{ch} \tag{4}$$

Here, n_i is the density of the species i, $\vec{\Gamma}_i$ the species flux, and k_{ij} the reaction rate. The indices ch, n, e, and ε denote charged species, neutral species, electrons, and the mean electron energy, respectively. μ is the mobility, D the diffusion constant and $\vec{E}$ the electric field. $k_{L,je}$ in eq. 3 represents the loss rate of the corresponding inelastic collision, m_e is the electron mass, m_{He} the mass of He, k_b the Boltzmann constant, v_m the elastic collision frequency, T_g the gas temperature, and T_e the electron tem-

perature ($\varepsilon = 3/2k_{\mathrm{b}}T_{\mathrm{e}}$). ϕ is the electric potential, ε_0 the vacuum permittivity, and q_{ch} the charge of species n_{ch}.

The ions are assumed to remain at the same energy (temperature) as the neutral background gas, thus the ion energy equation is not solved. Due to the high electric fields present in the plasma sheath, this assumption is not fulfilled in this region. To account for the higher ion temperature, the generalized Einstein relation is used for ion diffusivity, where the ion temperature is obtained using Wannier's formulation (5) [32].

$$k_{\mathrm{b}}T_{\mathrm{ion}} = k_{\mathrm{b}}T_{\mathrm{g}} + \frac{m_{\mathrm{ion}} + m_{\mathrm{He}}}{5m_{\mathrm{ion}} + 3m_{\mathrm{He}}} m_{\mathrm{He}} \left(\mu_{\mathrm{ion}} \left| \vec{E} \right| \right)^2 \tag{5}$$

The momentum conservation is written in the drift diffusion approximation, which is valid at elevated pressure. The main assumptions of this approximation are: The mean velocity of the particles does not change much over time, due to the high collision frequency; the distance the particles can travel between two collisions is small compared to the Debye length. The self-consistent model is closed by the boundary conditions for each considered species, potential, and electron energy. Helium and molecular oxygen are treated as background gases in the simulation with constant densities across the entire gap [29,33,34]. All other neutral species are kinetically limited at the electrodes of the jet. Helium metastables and excimers are assumed to be lost by de-excitation at the wall (unity surface quenching) [30,35].

$$\vec{\Gamma}_{\mathrm{n}}\vec{n} = \frac{1}{4}n_{\mathrm{n}}\sqrt{\frac{8k_{\mathrm{b}}T_{\mathrm{n}}}{\pi\, m_{\mathrm{n}}}} \tag{6}$$

Here, $\vec{n}$ is the normal vector on the electrode surface. The square root on the right-hand side represents the thermal velocity of the neutrals. The positive ions are assumed to be mobility limited at the surface, i.e., the drift term in eq. 2 is dominant and the diffusion term is neglected. For the mathematical description of this boundary, a switch function h_{s} is defined, which is one, if the ions are accelerated toward the surface, and zero otherwise (eq. 8). In addition, the ions have a thermal flux component to the surface. Here, unity surface recombination at the electrodes is assumed.

$$\vec{\Gamma}_{+}\vec{n} = h_{\mathrm{s}}\, \mu_{+}n_{+}\vec{E}\,\vec{n} + \frac{1}{4}n_{+}\sqrt{\frac{8k_{\mathrm{b}}T_{+}}{\pi\, m_{+}}} \tag{7}$$

$$h_{\mathrm{s}} = \begin{cases} 1 & \left(\vec{E}\cdot\vec{n} > 0 \right) \\ 0 & \left(\vec{E}\cdot\vec{n} \le 0 \right) \end{cases} \tag{8}$$

Here, the index + denotes positive ions. The electron flux toward the electrodes is given by the sum of thermal flux and flux of secondary electrons emitted from the electrodes. This gives rise to the electron energy flux as stated in eq. 10.

$$\vec{\Gamma}_{\mathrm{e}}\vec{n} = \frac{1}{4}n_{\mathrm{e}}\sqrt{\frac{8k_{\mathrm{b}}T_{\mathrm{e}}}{\pi\, m_{\mathrm{e}}}} - \sum_i \gamma \left(\vec{\Gamma}_i\vec{n} \right) \tag{9}$$

$$\vec{\Gamma}_{\varepsilon}\vec{n} = \frac{5}{3}\varepsilon\frac{1}{4}n_{\mathrm{e}}\sqrt{\frac{8k_{\mathrm{b}}T_{\mathrm{e}}}{\pi\, m_{\mathrm{e}}}} - \frac{5}{3}\varepsilon_\gamma \sum_i \gamma \left(\vec{\Gamma}_i\vec{n} \right) \tag{10}$$

Here, $\gamma = 0.1$ is the secondary electron emission coefficient and $\varepsilon_\gamma = 0.5$ eV is the assumed value for the energy of the secondary electrons after release from the electrodes [29].

The boundary condition of Poisson's equation incorporates the fact that one electrode is grounded and the other one is driven at a frequency of 13.56 MHz. Accordingly, the electric potential at the grounded electrode and at the powered electrode are set to

$$\phi_{gnd} = 0 \quad ; \quad \varphi_{pwr} = \varphi_0 \cos\left(2\pi ft\right) \tag{11}$$

where ϕ_0 denotes the amplitude of the potential and f the driving frequency. It is known that mode transitions occur in this type of capacitively coupled RF plasmas at atmospheric pressures [37]. In the transition region between the so-called α- and γ-mode, one can obtain multiple solutions for a fixed driving voltage. To cover the transition region and the corresponding multiple solutions, the power is specified rather than the potential at the powered electrode [30]. This can be done using a feedback loop. The total power coupled into the plasma during one RF cycle is calculated using eq. 12. Afterwards, the amplitude of the electrical potential at the powered electrode is adjusted proportional to the ratio of the actual and desired power (eq. 13).

$$P_{calc} = \frac{1}{T_{rf}} \int_{rf} \int_{vol} A \sum_{ch} q_{ch} \left(\vec{\Gamma}_{ch} \vec{E}\right) dxdt \tag{12}$$

$$\varphi_{0,new} = \varphi_{0,old} \left(\frac{P_{set}}{P_{calc}}\right)^c \quad ; \quad 0 < c \leq 1 \tag{13}$$

Here, P_{calc} is the calculated power coupled into the plasma per RF cycle and P_{set} the desired power. T_{rf} is the time interval of one RF cycle, A the electrode surface, $\phi_{0,new}$ the new amplitude, and $\phi_{0,old}$ the old amplitude of the electrical potential. The used transport coefficients for the described boundaries are summarized in Table 2. The described self-consistent model is solved using a time-dependent solver in COMSOL Multiphysics [38] in combination with MATLAB [39]. The timescales of the electron dynamics (several ns) and the plasma chemistry (several ms) are substantially different. Therefore, both are decoupled: Firstly, the complete set of partial differential equations is solved for several RF cycles; secondly, only the neutral species reactions are solved on a much longer time scale. This procedure is repeated until convergence is reached.

Table 2 Transport coefficients used in the numerical simulation.

Species	$\mu[m^2/Vs]$	$D[m^2/s]$	Ref.
e	$f(\varepsilon)$	$f(\varepsilon)$	[23]
He*	–	1.64×10^{-4}	[36]
He$^+$	1.31×10^{-3}	generalized Einstein relation	[32]
He$_2^*$	–	4.75×10^{-5}	[36]
He$_2^+$	1.83×10^{-3}	generalized Einstein relation	[32]
O$_2^+$	2.39×10^{-3}	generalized Einstein relation	[32]

$f(\varepsilon)$ indicates that the transport coefficients are calculated on the basis of the two-term approximation EEDF as a function of the mean electron energy.

Benchmark via PROES

As a benchmark for the model, a comparison with PROES measurements is used. This technique uses a fast intensified charge-coupled device (ICCD) camera with a high repetition rate of several MHz, collecting information over each RF cycle [40–44]. The emission is spectrally separated using an interference filter with a central wavelength of 750 nm and a FWHM of 10 nm. A defined gate width of 2 ns
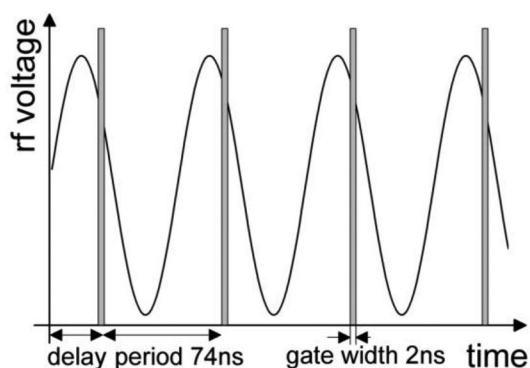
Fig. 4 Principle of the diagnostic technique PROES. Images are acquired during the 2 ns gates (marked in gray).

is used, and the gate time is shifted in 2 ns increments to sample the entire RF cycle, see Fig. 4. Integration over several million RF cycles yields a high signal-to-noise ratio.

Figure 5a shows the measured spatio-temporal optical emission characteristics of the argon lines at $\lambda = 750.4$ nm $(2p_1 \rightarrow 1s_2)$ and $\lambda = 751.5$ nm $(2p_5 \rightarrow 1s_1)$ across the discharge gap, for one RF cycle at a power of 59 W in helium with 0.5 % oxygen and 0.1 % argon admixtures. The dominant excitation structures observed display the sheath expansion and collapse. During sheath expansion, electrons are accelerated away from the electrode, whilst at the opposite electrode, the sheath collapse structure is induced by a field reversal effect, where an electric field build-up causes electrons to be accelerated toward the electrodes. This reversal is due to electrons colliding with the background gas, thus hindering them from responding to the rapid sheath movements. A third maximum is also observed within the plasma boundary sheath due to secondary electron multiplication in the high electric fields in this region. These secondary electrons are generated close to the electrode surfaces by the gamma effect, as well as through Penning ionization. This third structure is only present at higher powers, when the sheath electric field is high enough to generate an electron avalanche. The relative intensity of this third structure compared to the other two can be used to adjust the power used in the numerical simulation to the experiment. This is a delicate problem, since in the experiment the power coupled into the plasma is difficult to determine accurately, due to significant power losses in the RF equipment used, e.g., in the matching unit and connecting cables.

For comparison, Fig. 5b shows the simulated spatio-temporal characteristics of the argon optical emission line $\lambda = 750.4$ nm $(2p_1 \rightarrow 1s_2)$ across the electrode gap during one RF cycle for a voltage amplitude of 245 V (corresponding power: 0.33 W). The emission is determined by multiplying the simulated electron-impact excitation coefficient of the Ar($2p_1$) state with the time- and space-dependent electron density and integrating the resulting time dependence to account for the effective lifetime of the upper state. Cascade processes populating the Ar($2p_1$) state are in general comparatively small [26]. At atmospheric pressure, cascade processes can be assumed to be even smaller due to very effective collisional quenching of the upper level. This allows us to neglect cascading processes for the population of the Ar($2p1$) state. In each half cycle, the same three emission maxima are observed at the same temporal and spatial positions as in the PROES experiments. Although a relatively good comparison between simulation and experiment is shown, the emission in the discharge center is clearly more pronounced in the experimental results. One possible explanation is that the interference filter used is not able to spectrally separate the close-by Ar($2p_1$) and Ar($2p_5$) emission lines. The Ar($2p_5$) state is known to be additionally populated by electron-impact excitation out of the Ar($1s_5$) metastable state. This process, due to its low threshold energy, is primarily driven by low energetic electrons which are mainly
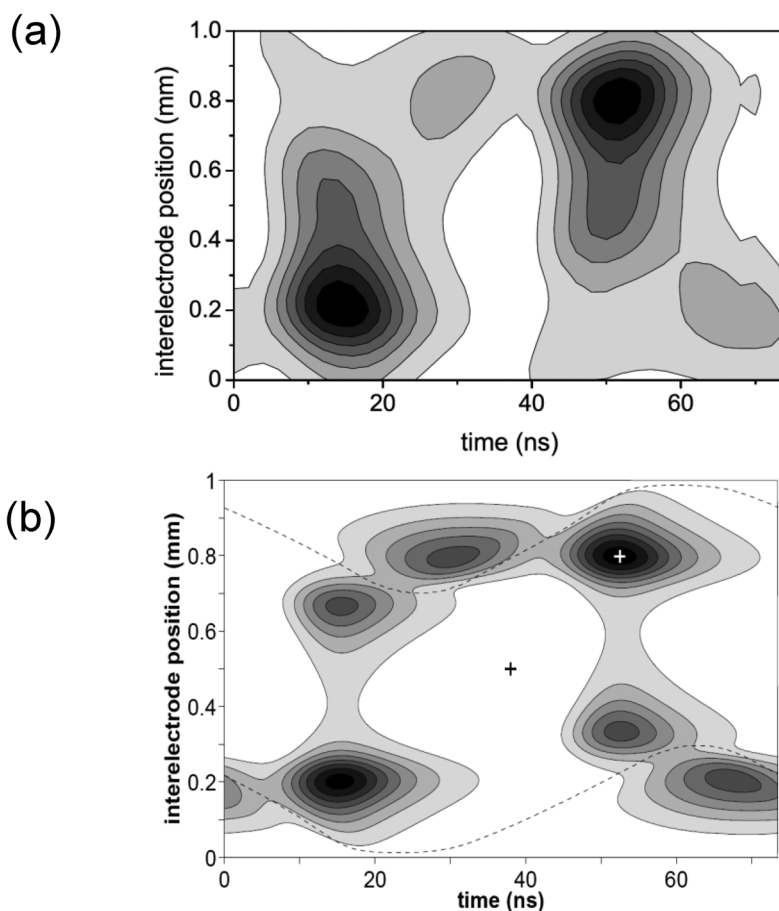
Fig. 5 (a) PROES measurement of the sum emission pattern of the Ar($2p_1$) and Ar($2p_5$) lines and (b) numerical simulation of the emission pattern of the Ar($2p_1$) line within one RF cycle. The dashed lines indicate the position of the sheath edges.

present in the plasma bulk. However, the emission from the Ar($2p_5$) state cannot be simulated here, since information on the Ar($1s_5$) metastable density is missing.

DBM results

The resulting time- and space-averaged EEDF obtained by the benchmarked numerical simulation is shown in Fig. 6 as a solid line. The dashed lines show two EEDFs at points of minimal and maximal excitation (also illustrated by crosses in Fig. 5b). The averaged EEDF is used to calculate the effective excitation rate coefficients k_e^* according to $k_e^* = \langle n_e \rangle^{-1}_{x,t} \int \langle n_e f(\varepsilon) \rangle_{x,t} \sigma(\varepsilon) v_e \, d\varepsilon$, where $\sigma(\varepsilon)$ is the excitation cross-section and v_e is the electron velocity. The effective excitation rates describe the time- and space-integrated optical emission measurements adequately. The calculation yields an electron-impact excitation ratio of $k_{Ar,e}^* / k_{O,e}^* = 0.32$ (see Fig. 3).

The dissociative electron-impact excitation process e + $O_2 \rightarrow$ O ($3p^3P$) + O + e, not included in the classical actinometry approach, has a higher threshold of 16.3 eV than the direct excitation process. Also, the maximum is smaller and at far higher electron energies. Nevertheless, at lower dissociation degrees, the dissociative excitation becomes relevant or even dominant and needs to be taken into account [13]. For a quantitative density determination, which includes the dissociative excitation process
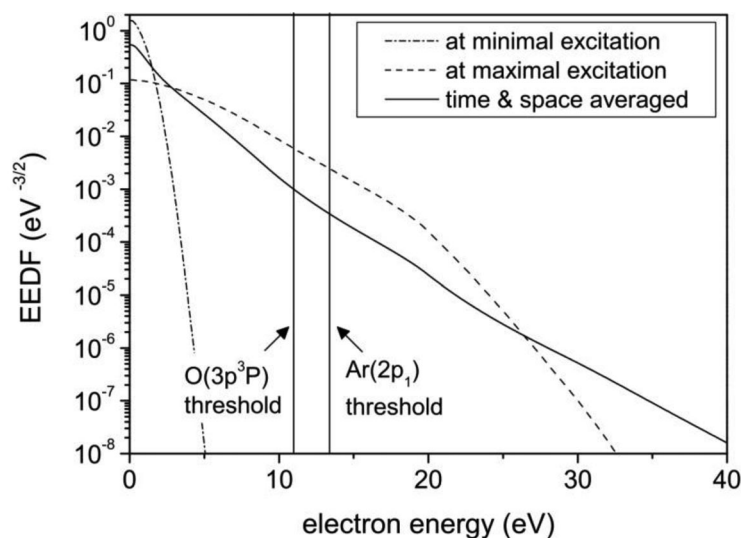
Fig. 6 Calculated EEDF. Crosses in Fig. 5b mark time and space of minimal and maximal excitation.

above, detailed information on the EEDF in the relevant energy range is required. The calculated effective excitation rate ratios for the direct excitation channel (index e) and the dissociative excitation channel (index de) are $k_{Ar,e}^{*}/k_{O,e}^{*} = 0.32$ and $k_{O,de}^{*}/k_{O,e}^{*} = 9 \times 10^{-3}$. Regarding the consequences of the reduced model (17 reactions) on the excitation rate ratio, a comparative evaluation with an extended model (57 reactions) shows a difference of below 3 %. The EEDF in the range of the excitation thresholds is largely independent of the chemical reactions. The O-atom density is finally evaluated according to

$$n_{O} = \frac{I_{O} h \nu_{Ar} k_{Ar,e}^{*} a_{Ar}}{I_{Ar} h \nu_{O} k_{O,e}^{*} a_{O}} n_{Ar} - \frac{k_{O,de}^{*}}{k_{O,e}^{*}} n_{O_2} \tag{14}$$

Figure 7 shows the resulting atomic oxygen density along the discharge channel of the μAPPJ. The nozzle of the jet defines the zero position and the gas inlet is at $z = -30$ mm. The atomic oxygen density increases from 1.4×10^{16} cm^{-3} over a distance of 10 mm and approaches a relatively constant value of 1.7×10^{16} cm^{-3}, indicating that the destruction and production processes of atomic oxygen balance. This equilibrium is reached corresponding to the gas speed of 17 m/s after 0.6 ms. The intensity of the argon optical emission line $\lambda = 750.4$ nm ($2p_1 \rightarrow 1s_2$) probing the electron properties remains relatively constant after the first 2 mm of the discharge, after 0.12 ms correspondingly, indicating that the core plasma is homogeneous. The build-up of the atomic oxygen production and destruction equilibrium is therefore to be attributed to slow chemical reactions rather than to fast electron-induced processes. At 10 mm distance to the nozzle, the O-atom density as well as the argon emission starts to decrease. This effect is most likely caused by back-diffusion of ambient air species from the nozzle into the plasma.
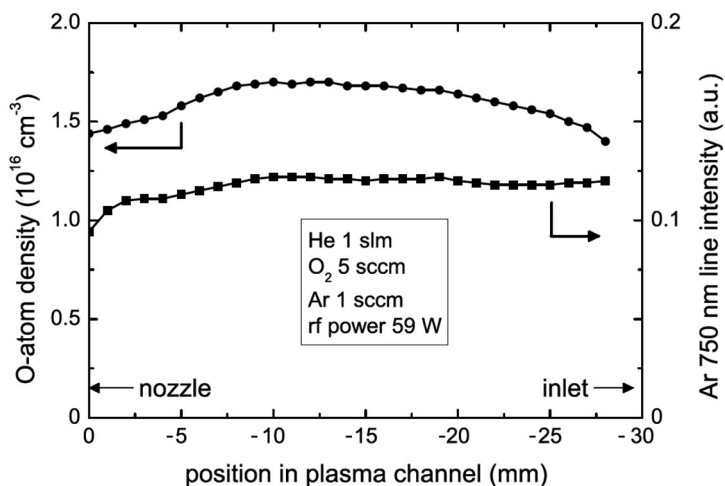
Fig. 7 O atom density and Ar 750 nm line intensity as a function of the position within the discharge channel.

A similar behavior has been determined by TALIF measurements on a similar set-up with an electrode spacing of 2 mm in helium with an admixture of 0.5 % oxygen at 40 W [18]: Here, the balance of oxygen chemistry is reached after about 8 mm corresponding to 1 ms at a gas speed of 10 m/s as can be seen in Fig. 8. Here, the absolute atomic oxygen density measured by TALIF is shown from the gas inlet at $z = -30$ mm up to the center of the discharge channel at $z = -15$ mm. The maximum density of 1.7×10^{16} cm^{-3} in the center coincides with the value found from the OES measurement.
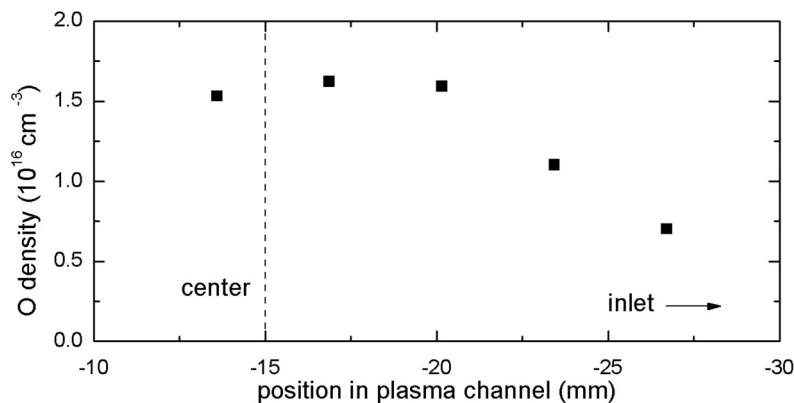

Fig. 8 TALIF measurements inside a µAPPJ with 2 mm electrode gap. Axial profile of absolute O atom density at 40 W RF generator power in He with an 0.5 % O$_2$ admixture.

The operational power differs slightly, because it depends on the RF equipment used. A higher maximal O-atom density is found in the TALIF investigation: 2.7×10^{16} cm^{-3} at 54 W in comparison to 2.1×10^{16} cm^{-3} at 62 W in the OES set-up. Most probably, this reflects the different surface-to-volume ratios of the investigated discharges due to a different gap size. Additionally, the TALIF measurement probes the higher O-atom density on the axis of the discharge, where the OES measurement, on the other hand, yields the space-averaged value comprising all effective particle losses toward the surrounding surfaces.

ACKNOWLEDGMENTS

REFERENCES

1. E. Stoffels, I. E. Kieft, R. E. J. Sladek, L. J. M. van den Bedem, E. P. van der Laan, M. Steinbuch. *Plasma Sources Sci. Technol.* **15**, S169 (2006).
2. R. Foest, E. Kindel, H. Lange, A. Ohl, M. Stieber, K.-D. Weltmann. *Contrib. Plasma Phys.* **47**, 119 (2007).
3. K. Becker, A. Koutsospyros, S. M. Yin, C. Christodoulatos, N. Abramzon, J. C. Joaquin, G. Brelles-Marino. *Plasma Phys. Controlled Fusion* **47**, B513 (2005).
4. K.-D. Weltmann, R. Brandenburg, T. von Woedtke, J. Ehlbeck, R. Foest, M. Stieber, E. Kindel. *J. Phys. D: Appl. Phys.* **41**, 194008 (2008).
5. A. Schütze, J. Y. Jeong, S. E. Babayan, J. Park, G. S. Selwyn, R. F. Hicks. *IEEE Trans. Plasma Sci.* **26**, 1685 (1998).
6. K. Niemi, St. Reuter, L. Schaper, N. Knake, V. Schulz-von der Gathen, T. Gans. *J. Phys.: Conf. Series* **71**, 012012 (2007).
7. V. Schulz-von der Gathen, V. Buck, T. Gans, N. Knake, K. Niemi, S. Reuter, L. Schaper, J. Winter. *Contrib. Plasma Phys.* **47**, 510 (2007).
8. J. Y. Jeong, J. Park, I. Henins, S. E. Babayan, V. J. Tu, G. S. Selwyn, G. Ding, R. F. Hicks. *J. Phys. Chem. A* **104**, 8027 (2000).
9. V. Schulz-von der Gathen, L. Schaper, N. Knake, St. Reuter, K. Niemi, T. Gans, J. Winter. *J. Phys. D: Appl. Phys.* **41**, 194004 (2008).
10. M. Geigl, S. Peters, O. Gabriel, B. Krames, J. Meichsner. *Contrib. Plasma Phys.* **45**, 369 (2005).
11. K. Niemi, V. Schulz-von der Gathen, H. F. Döbele. *Plasma Sources Sci. Technol.* **14**, 375 (2005).
12. J. W. Coburn, M. Chen. *J. Appl. Phys.* **51**, 3134 (1980).
13. R. E. Walkup, K. L. Saenger, G. S. Selwyn. *J. Chem. Phys.* **84**, 2668 (1986).
14. H. M. Katsch, A. Tewes, E. Quandt, A. Goehlich, T. Kawetzki, H. F. Döbele. *J. Appl. Phys.* **88**, 6232 (2000).
15. G. Park, H. Lee, G. Kim, J. K. Lee. *Plasma Processes Polym.* **5**, 569 (2008).
16. S. Reuter, K. Niemi, V. Schulz-von der Gathen, H. F. Döbele. *Plasma Sources Sci. Technol.* **18**, 015006 (2009).
17. N. Knake, S. Reuter, K. Niemi, V. Schulz-von der Gathen, J. Winter. *J. Phys. D: Appl. Phys.* **41**, 194006 (2008).
18. N. Knake, K. Niemi, S. Reuter, V. Schulz-von der Gathen, J. Winter. *Appl. Phys. Lett.* **93**, 131503 (2008).
19. J. J. Shi, M. G. Kong. *J. Appl. Phys.* **97**, 023306 (2005).
20. C. M. O. Mahony, T. Gans, W. G. Graham, P. D. Maguire, Z. Lj. Petrović. *Appl. Phys. Lett.* **93**, 011501 (2008).
21. K. Niemi, S. Reuter, L. M. Graham, J. Waskoenig, T. Gans. *Appl. Phys. Lett.* **95**, 151504 (2009).
22. K. Niemi, S. Reuter, L. M. Graham, J. Waskoenig, N. Knake, V. Schulz-von der Gathen, T. Gans. *J. Phys. D: Appl. Phys.* **43**, 124006 (2010).
23. G. J. M. Hagelaar, L. C. Pitchford. *Plasma Sources Sci. Technol.* **14**, 722 (2005).
24. G. S. Selwyn, H. W. Herrmann, J. Park, I. Henins. *Contrib. Plasma Phys.* **6**, 610 (2001).

25. N. Sadeghi, D. W. Setser, A. Francis, U. Czarnetzki, H. F. Döbele. *J. Chem. Phys.* **115**, 3144 (2001).
26. J. E. Chilton, J. B. Boffard, R. S. Schappe, C. C. Lin. *Phys. Rev. A* **57**, 267 (1998).
27. M. B. Schulman, F. A. Scharpton, S. Chung, C. C. Lin, L. W. Anderson. *Phys. Rev. A* **32**, 2100 (1985).
28. L. L. Laher, F. R. Gilmore. *J. Phys. Chem. Ref. Data* **19**, 277 (1990).
29. X. Yuan, L. L. Raja. *IEEE Trans. Plasma Sci.* **31**, 495 (2003).
30. Y. Sakiyama, D. B. Graves. *J. Phys. D: Appl. Phys.* **39**, 3644 (2006).
31. D. S. Stafford, M. J. Kushner. *J. Appl. Phys.* **96**, 2451 (2004).
32. H. W. Ellis, R. Y. Pai, W. McDaniel, E. A. Mason, L. A. Viehland. *At. Data Nucl. Data Tables* **17**, 177 (1976).
33. Y. Sakiyama, D. B. Graves. *J. Appl. Phys.* **101**, 073306 (2007).
34. J. J. Shi, M. G. Kong. *J. Appl. Phys.* **97**, 023306 (2005).
35. K. De Bleecker, D. Herrebout, A. Bogaerts, R Gijbels, P. Descamps. *J. Phys. D: Appl. Phys.* **36**, 1826 (2003).
36. R. J. Kee, G. Dixon-Lewis, J. Warnatz, M. E. Coltrin, J. M. Miller. *Sandia Report SAND86*-8246 (1986).
37. J. J. Shi, M. Kong. *IEEE Trans. Plasma Sci.* **33**, 624 (2005).
38. Comsol Multiphysics 3.4. Herfordshire, AL10 9AB: COMSOL Ltd. (2007).
39. Matlab 7.5. MathWorks, Natick, MA (2007).
40. T. Gans, Chun C. Lin, V. Schulz-von der Gathen, H. F. Döbele. *Phys. Rev. A* **67**, 012707 (2003).
41. K. Dittmann, D. Drozdov, B. Krames, J. Meichsner. *J. Phys. D: Appl. Phys.* **40**, 6593 (2007).
42. L. Schaper, S. Reuter, J. Waskoenig, K. Niemi, V. Schulz-von der Gathen, T. Gans. *J. Phys.: Conf. Series* **162**, 012013 (2009).
43. J. Waskoenig, D. O'Connell, V. Schulz-von der Gathen, J. Winter, S.-J. Park, J. G. Eden. *Appl. Phys. Lett.* **92**, 101503 (2008).
44. H. Boettner, J. Waskoenig, D. O'Connell, T. L. Kim, P. A. Tchertchian, J. Winter, V. Schulz-von der Gathen. *J. Phys. D: Appl. Phys.* **43**, 124010 (2010).